Modification of thermoelectric properties in $Ca_3Co_4O_y$ ceramics by Nd doping

G. Constantinescu[1], M. A. Torres[2], Sh. Rasekh[1], M. A. Madre[1], J. C. Diez[1], A. Sotelo[1]

[1]ICMA (UZ-CSIC), Dpto. de Ciencia y Tecnología de Materiales y Fluidos, C/María de Luna 3, E-50018, Zaragoza (Spain)

[2]Universidad de Zaragoza, Dpto. de Ingeniería de Diseño y Fabricación, C/María de Luna 3, E-50018, Zaragoza (Spain)

Abstract

$Ca_{3-x}Nd_xCo_4O_y$ polycrystalline thermoelectric ceramics with small amounts of Nd have been synthesized by the classical solid state method. XRD data have shown that all the Nd has been incorporated into the $Ca_3Co_4O_9$ and $Ca_3Co_2O_6$ phases and no Nd-containing secondary phases have been produced. Apparent density measurements have revealed that all samples are very similar, with densities around 70 % of the theoretical one. Electrical resistivity decreases in all Nd-doped samples, compared with the pure one, while Seebeck coefficient remains constant for all samples. The improvement in resistivity leads to higher power factor values than the obtained for the undoped samples.

Keywords: Ceramics; Cobaltites; Electrical properties; Thermopower.

Corresponding author: M. A. Madre

e-mail: amadre@unizar.es

Address: Dept. Ciencia de Materiales; C/Mª de Luna, 3; 50018-Zaragoza; Spain

Tel: +34 976762617

Fax: +34 976761957

1. Introduction

Thermoelectric (TE) materials can directly transform a temperature difference to electrical power due to the well-known Seebeck effect. The conversion efficiency is quantified by the dimensionless figure of merit ZT, $TS^2/\rho\kappa$ (S^2/ρ is called power factor, PF), where S is Seebeck coefficient, ρ electrical resistivity, κ thermal conductivity, and T is the absolute temperature [1]. These characteristics have focused attention on these materials in order to be used in several applications as waste heat recovery devices [2] or solar thermoelectric generators [3]. Furthermore, they can also be used as heating/refrigeration devices [4].

Nowadays TE devices based on intermetallic materials are industrially used, e.g. in vehicles exhaust. However, due to their degradation under air at high temperatures, they cannot be applied in devices working in these conditions. These limitations were overwhelmed by the discovery of high thermoelectric properties in $Na_2Co_2O_4$ ceramics [5]. Since then, much work has been performed on the cobalt-based ceramics for high temperature applications, leading to the discovery and optimization of new compositions, such as $Ca_3Co_4O_9$ [6,7] $Bi_2Sr_2Co_2O_x$ [8,9], $Bi_2Ca_2Co_2O_x$ [10,11] and $Bi_2Ba_2Co_2O_x$ [12,13] with high thermoelectric properties and working temperatures.

Crystallographic studies have demonstrated that these materials possess a monoclinic structure which is, in turn, composed of two different layers. These layers show an alternate stacking of a common conductive CdI_2-type hexagonal CoO_2 layer with a two-dimensional triangular lattice and a block layer composed of insulating rock-salt-type (RS) layers. The two sublattices (RS block and CdI_2-type CoO_2 layer) possess common a- and c-axis lattice parameters and β

angles, but different b-axis length, causing a misfit along the b-direction [14]. The high structural anisotropy of these materials leads to the formation of plate-like grains during the crystallisation process which opens the route to preferentially align the grains using physical, mechanical and/or chemical processes. Such processes allow the alignment of the conducting planes leading to macroscopic properties comparable to those obtained on single crystals. Numerous methods have been reported to be efficient to produce well aligned bulk materials, in these or in similar anisotropic systems, such as hot uniaxial pressing [15], spark plasma sintering [16], microwave texturing [17], laser floating zone melting (LFZ) [18], electrically assisted laser floating zone [19], *etc*. The main drawbacks of these methods are due to different factors, as the relatively long treatments, the high costs associated with the processes and/or the strong dependence on the growth or the texturing speed [13,17,20-22].

It has also been reported that the Seebeck coefficient values are governed by the incommensurability ratio and/or the charge of the RS block layer between the CoO_2 ones [23] which provides the basis for the modification of thermoelectric properties by doping. The most common ones are based on the substitution of an alkaline-earth [24,25], Co [26,27], or Bi [28,29].

The aim of this work is to study the effect of Nd^{3+} for Ca^{2+} small substitutions on the microstructure and high temperature thermoelectric properties of $Ca_{3-x}Nd_xCo_4O_y$ prepared by the classical solid state synthetic route.

2. Experimental

$Ca_{3-x}Nd_xCo_4O_y$ polycrystalline ceramic materials, with x = 0.00, 0.01, 0.03, and 0.05, were prepared by the conventional solid state route using commercial $CaCO_3$ (Panreac, 98 + %), Co_2O_3 (Aldrich, 98 + %), and Nd_2O_3 (Aldrich, 99.9 %) powders as starting materials. They were weighed in the appropriate proportions, mixed and ball milled for 30 minutes at 300 rpm, in acetone media, in an agate ball mill. The slurry has been heated under infrared radiation until all the acetone has been evaporated. The dry mixture was then manually milled and thermally treated twice at 750 and 800 ºC for 12h under air, with an intermediate manual grinding to assure the total decomposition of $CaCO_3$, as reported previously [7]. After thermal treatment, the powders were uniaxially pressed at 400 MPa for 1 minute in order to obtain green ceramic parallelepipeds (~ 3 mm x 3 mm x 14 mm) and sintered at 910 ºC for 24 h with a final furnace cooling.

Powder X-ray diffraction (XRD) patterns have been systematically recorded in order to identify the different phases in the thermoelectric sintered materials. Data have been collected at room temperature, with 2θ ranging between 5 and 60 degrees, using a Rigaku D/max-B X-ray powder diffractometer working with Cu Kα radiation.

Microstructural observations were performed on longitudinal polished sections of the samples, using a Field Emission Scanning Electron Microscope (FESEM, Carl Zeiss Merlin) fitted with an energy dispersive spectrometry (EDS) device. Micrographs of polished sections of the samples have been used to analyze the different phases and their distribution. Apparent density measurements have been performed on several samples for each composition after sintering, using 4.677 g/cm^3 as theoretical density [30].

Electrical resistivity and Seebeck coefficient were simultaneously determined by the standard dc four-probe technique in a LSR-3 measurement system (Linseis GmbH), in the steady state mode and at temperatures ranging from 50 to 800 ºC under He atmosphere. With the electrical resistivity and thermopower data, the power factor has been calculated in order to determine the samples performances. These properties have been compared with the results obtained in undoped samples and with those reported in the literature.

3. Results and discussion

Powder XRD patterns for the different $Ca_{3-x}Nd_xCo_4O_y$ samples are displayed in Fig. 1 (from 5 to 40º for clarity). From these data, it is clear that all the samples have very similar diffraction patterns. As can be seen in Fig. 1a, corresponding to the undoped samples, the highest peaks have been associated to the thermoelectric $Ca_3Co_4O_9$ phase, indicated by the reflection planes, in agreement with previously reported data [31]. On the other hand, the peak at around 28.65 degrees (indicated by # in Fig. 1d) corresponds to the (111) diffraction plane of Si used as reference. When Nd is added to the samples, some new peaks appear (identified by * in Fig 1d) which have been associated to the $Ca_3Co_2O_6$ phase, in agreement with previously reported data [31]. When focusing in these peaks, it can be seen a slight increase on their intensity, indicating that $Ca_3Co_2O_6$ phase content increases when the amount of Nd is raised. All these observations indicate that all the samples are composed by $Ca_3Co_4O_9$ as the major phase, accompanied by small amounts of $Ca_3Co_2O_6$. This is a clear indication that all added Nd has been incorporated in the $Ca_3Co_4O_9$ and $Ca_3Co_2O_6$ structures as no other Nd-containing phases are

detected. Moreover, no shift on the $Ca_3Co_4O_9$ peaks has been detected due to the small amount of Nd and the small difference in the relative size between Ca and Nd.

General SEM observations performed on representative polished sections have shown that porosity seems to slightly increase when Nd content is raised, as illustrated in Fig. 2 where representative views of all the samples are displayed. On the other hand, it is clear that Nd addition produces the formation of a new contrast in the samples (white one) with higher proportions as Nd content is increased. EDS analysis have shown that the grey contrast (#1 in Fig. 2a) corresponds to the $Ca_3Co_4O_9$ phase. As it can be observed in the figure, this phase is the major one in all samples and possesses different amounts of Nd in its composition depending on the Nd nominal composition. The white phase (#2 in Fig. 2d) corresponds to a Nd-rich $Ca_3Co_2O_6$ phase, with Nd contents which can reach 0.1 for the 0.05 Nd-doped samples. The calculated composition for the different phases and contrasts are displayed in Table I. These microstructural observations are in agreement with the XRD data which show an increase of the $Ca_3Co_2O_6$ phase when the Nd content is raised.

In order to check the effect of Nd content on the porosity of the bulk sintered materials, apparent density measurements have been performed for all samples. At least three samples for each composition were measured for three times to minimize measurement errors. The obtained mean values, together with their standard error, are represented in Fig. 3. As it can be clearly seen in the figure, the density values slightly decrease following an exponential trend when Nd content is increased. This evolution is in agreement with the microstructural observations discussed previously. On the other hand, when

considering the relative density, compared with the theoretical one, the values are ranging from around 72 % for the pure samples, to about 70 % for the 0.05 Nd-substituted ones, confirming the small changes on the porosity observed in the SEM micrographs.

Fig. 4 shows the variation of the Seebeck coefficient with the temperature, as a function of the Nd doping. In the plot, it can be clearly seen that the sign of the thermopower is positive for the entire measured temperature range, which confirms a conduction mechanism mainly governed by holes. The values of the Seebeck coefficient increase with the temperature, with very similar values and behaviour for all the samples. The obtained values at room temperature (~ 135 μV/K) are slightly higher than those reported elsewhere (~ 125 μV/K) at the same temperature [32]. On the other hand, the maximum Seebeck coefficient value (~ 210 μV/K) obtained in this work at 800 ºC is significantly higher than the best values obtained for $Ca_3Co_4O_9$ samples consolidated by spark plasma sintering (170-175 μV/K) at about 625 ºC [33]. The similar values obtained for all samples indicate that small Nd addition does not affect, in a great extent, the $Ca_3Co_4O_9$ conduction band [27].

The temperature dependence of electrical resistivity, as a function of the Nd content, is shown in Fig. 5. The ρ (T) curves show a decrease of resistivity when Nd is added, compared with the undoped samples. All the curves show a semiconducting-like ($d\rho/dT < 0$) behaviour, from room temperature to around 400 ºC, in agreement with previously reported data in this system where the charge transport process is a hole hopping from Co^{4+} to Co^{3+} [34]. At higher temperatures, this behaviour changes to a metallic-like ($d\rho/dT > 0$) one where the charge carriers are transported in the valence or conduction band [35]. In

these doped samples, room temperature resistivity values decrease in an important manner (~ 25 %, compared with the undoped one) for 0.01 Nd substitution, and then increases with the Nd content. In any case, the lowest measured room temperature resistivity values (~ 16 mΩ.cm for the 0.01 Nd-substituted samples) is around the best values obtained for $Ca_3Co_4O_9$ samples produced by no so simple and cheap methods. As examples, it can be considered the values obtained in samples consolidated by spark plasma sintering (15-18 mΩ.cm) [33] or produced by solution methods (~ 16 mΩ.cm) [7]. Taking into account that density values are decreasing with increasing the Nd-contents, the electrical resistivity evolution can be most probably explained by the modification of the carrier concentration, when Nd is added to the $Ca_3Co_4O_9$ samples. On the other hand, the increase on the resistivity values for higher Nd-content should be due to the decrease on the density values, together with the higher amount of secondary phases (mainly $Ca_3Co_2O_6$) produced by the Nd addition. This increase on the secondary phases reduces the amount of $Ca_3Co_4O_9$ phase and reducing the effective path for the electrical transport. Moreover, the electrical resistivity of $Ca_3Co_2O_6$ (~ 500 Ω.cm) [36] is much higher than the obtained in $Ca_3Co_4O_9$ (between 15 and 18 mΩ.cm) [33]. As a consequence, the bulk resistivity should be raised with the increase of $Ca_3Co_2O_6$ phase if no other factors are influencing the samples behaviour at the same time.

In order to check the validity of our hypothesis about the increase on the carrier concentration when samples are doped with Nd, the ln (σT) *vs.* $1/k_BT$ Arrhenius plot has been made and represented in Fig. 6. In these compounds, the charge-

transport process is produced by a hole hopping from Co^{4+} to Co^{3+} [34] and the temperature dependence of the electrical conductivity can be described as:

$\sigma.T \propto \exp (E/k_B.T)$

where E, k_B, and T are the activation energy, Boltzmann constant, and absolute temperature, respectively. The activation energy values are obtained from the ln (σT) *vs.* $1/k_BT$ plot as the curve fit slope in the different samples below T*, as illustrated in Fig. 6. T* is defined as the temperature where the behaviour of the samples changes from semiconducting to metallic one, slightly lower for the Nd doped samples (indicated by T_1*) than for the pure ones (indicated by T_2*). The activation energy calculated values have been found to be around 40 meV in all cases, confirming that Nd addition does not modify appreciably the $Ca_3Co_4O_9$ conduction band. On the other hand, the carrier concentration is clearly modified by Nd addition, as can be easily seen in the insert of Fig. 6. In the insert it is obvious that all Nd-added samples increase their carrier concentration, compared with the Nd-free ones, when considering that only a slight modification in the carrier mobility is produced. The maximum increase is obtained for the 0.01 Nd-doped samples in around 25-30 % higher than for the pure ones, slightly decreasing for further Nd addition.

In order to evaluate the thermoelectric performances of these materials, the power factor has been calculated. The temperature dependence of the power factor has been calculated using the data displayed in Figs. 4 and 5 and plotted in Fig. 7. When considering PF values at around 50 ºC (~ room temperature), it can be clearly seen that the Nd-doped samples possess higher PF values than the undoped ones (around 20 %). The highest PF value obtained at 800 ºC (around 0.26 $mW/K^2.m$) for the 0.01 Nd-doped samples is about 30 % higher

than the obtained for the undoped samples. In all cases, the PF values are much higher than the obtained in samples with higher Nd-doping reported in the literature [37]. This improvement is only due to the important decrease on the electrical resistivity, discussed previously, as all the samples possess practically the same Seebeck coefficient values.

All the obtained data show that small Nd additions can improve significantly the thermoelectric performances of $Ca_3Co_4O_9$ ceramics, thus approaching them for next future practical applications.

4. Conclusions

This paper demonstrates that small Nd additions to $Ca_3Co_4O_9$ samples improve their thermoelectric properties. Nd addition benefits the electrical conductivity of the samples without appreciably modifying the Seebeck coefficient values. The optimal Nd for Ca substitution has been determined using the values of the power factor at 50 and 800 ºC, which is maximum for the 0.01 Nd-doped samples with values around 0.11 and 0.26 $mW/K^2.m$, respectively, which are about 30 % higher than the obtained for the undoped samples. This important raise of PF is most probably caused by the increase of the carrier concentration, leading to a decrease of electrical resistivity of about 25 % compared with the values obtained in undoped samples.

Acknowledgements

The authors wish to thank the Gobierno de Aragón (Research Groups T12 and T87) for financial support. The technical contributions of C. Estepa, and C.

Gallego are also acknowledged. Sh. Rasekh acknowledges a JAE-PreDoc 2010 grant from CSIC.

References

1. D. M. Rowe, in Thermoelectrics handbook: macro to nano, ed By D. M. Rowe (CRC Press, Boca Raton, FL, 2006) p. 1-3

2. G. Mahan, B. Sales, J. Sharp, Phys. Today 50, 42 (1997)

3. H. Naito, Y. Kohsaka, D. Cooke, H. Arashi, Solar Energy 58, 191 (1996)

4. C. M. Kim, Y. J. Hwang, Y. H. Ryu, US Patent US6393842. May, 2002.

5. I. Terasaki, Y. Sasago, K. Uchinokura, Phys. Rev. B 56, 12685 (1997)

6. Y. Huang, B. Zhao, J. Fang, R. Ang, Y. Sun, J. Appl. Phys. 110, 123713 (2011)

7. A. Sotelo, G. Constantinescu, Sh. Rasekh, M. A. Torres, J. C. Diez, M. A. Madre, J. Eur. Ceram. Soc. 32, 2415 (2012)

8. N. Sun, S. T. Dong, B. B. Zhang, Y. B. Chen, J. Zhou, S. T. Zhang, Z. B. Gu, S. H. Yao, Y. F. Chen, J. Appl. Phys. 114, 043705 (2013)

9. J. C. Diez, E. Guilmeau, M. A. Madre, S. Marinel, S. Lemmonier, A. Sotelo, Solid State Ionics 180, 827 (2009)

10. X. G. Luo, Y. C. Jing, H. Chen, X. H. Chen, J. Crystal Growth 308, 309 (2007)

11. A. Sotelo, E. Guilmeau, Sh. Rasekh, M. A. Madre, S. Marinel, J. C. Diez, J. Eur. Ceram. Soc. 30, 1815 (2010)

12. R. Ang, Y. P. Sun, X. Luo, W. H. Song, J. Appl. Phys. 102, 073721 (2007)

13. Sh. Rasekh, G. Constantinescu, M. A. Torres, M. A. Madre, J. C. Diez, A. Sotelo, Adv. Appl. Ceram. 111, 490 (2012)

14. Y. Miyazaki, Solid State Ionics 172, 463 (2004)

15. H. Wang, X. Sun, X. Yan, D. Huo, X. Li, J.-G. Li, X. Ding, J. Alloys Compds. 582, 294 (2014)

16. J. G. Noudem, D. Kenfaui, D. Chateigner, M. Gomina, J. Electronic. Mater. 40, 1100 (2011)

17. S. Marinel, D. Bourgault, O. Belmont, A. Sotelo, G. Desgardin, Physica C 315, 205 (1999)

18. A. Sotelo, E. Guilmeau, M. A. Madre, S. Marinel, J. C. Diez, M. Prevel, J. Eur. Ceram. Soc. 27, 3697 (2007)

19. N. M. Ferreira, Sh. Rasekh, F. M. Costa, M. A. Madre, A. Sotelo, J.C. Diez, M. A. Torres, Mater. Lett. 83, 144 (2012)

20. A. Sotelo, E. Guilmeau, M. A. Madre, S. Marinel, S. Lemmonier, J. C. Diez, Bol. Soc. Esp. Ceram. V. 47, 225 (2008)

21. J. C. Diez, Sh. Rasekh, M. A. Madre, E. Guilmeau, S. Marinel, A. Sotelo, J. Electron. Mater. 39, 1601 (2010)

22. G. Constantinescu, Sh. Rasekh, M. A. Torres, M. A. Madre, J. C. Diez, A. Sotelo, Scripta Mater. 68, 75 (2013)

23. A. Maignan, D. Pelloquin, S. Hébert, Y. Klein, M. Hervieu, Bol. Soc. Esp. Ceram. V. 45, 122 (2006)

24. G. Constantinescu, Sh. Rasekh, M. A. Torres, J. C. Diez, M. A. Madre, A. Sotelo, J. Alloys Compds. 577, 511 (2013)

25. S. Demirel, M. A. Aksan, S. Altin, J. Mater. Sci.: Mater. Electron. 23, 2251 (2012)

26. J. C. Diez, M. A. Torres, Sh. Rasekh, G. Constantinescu, M. A. Madre, A. Sotelo, Ceram. Int. 39, 6051 (2013)

27. Sh. Rasekh, M. A. Torres, G. Constantinescu, M. A. Madre, J. C. Diez, A. Sotelo, J. Mater. Sci.: Mater. Electron. 24, 2309 (2013)

28. A. Sotelo, Sh. Rasekh, E. Guilmeau, M. A. Madre, M. A. Torres, S. Marinel, J. C. Diez, Mater. Res. Bull. 46, 2537 (2011)

29. M. A. Madre, M. A. Torres, Sh. Rasekh, J. C. Diez, A. Sotelo, Mater. Lett. 75, 5 (2012)

30. M. A. Madre, F. M. Costa, N. M. Ferreira, A. Sotelo, M. A. Torres, G. Constantinescu, Sh. Rasekh, J. C. Diez, J. Eur. Ceram. Soc. 33, 1747 (2013)

31. E. Woermann, A. Muan, J. Inorg. Nucl. Chem. 32, 1455 (1970)

32. Y. Wang, Y. Sui, X. Wang, W. Su, X. Liu, J. Appl. Phys. 107, 033708 (2010)

33. D. Kenfaui, G. Bonnefont, D. Chateigner, G. Fantozzi, M. Gomina, J. G. Noudem, Mater. Res. Bull. 45, 1240 (2010)

34. Y. H. Lin, J. Lan, Z. J. Shen, Y. H. Liu, C. W. Nan, J. F. Li, Appl. Phys. Lett. 94, 072107 (2009)

35. S. Pinitsoontorn, N. Lerssongkram, N. Keawprak, V. Amornkitbamrung, J. Mater. Sci.: Mater. Electron. 23, 1050 (2012)

36. M. Senthilkumar, R. Vijayaraghavan, Sci. Technol. Adv. Mater. 10, 015007 (2009)

37. M. Prevel, E. S. Reddy, O. Perez, W. Kobayashi, I. Terasaki, C. Goupil, J. G. Noudem, Jpn. J. Appl. Phys. 46, 6533 (2007)

Table I. Calculated composition of the different phases and contrasts from the EDS analysis using Ca content as reference.

Sample	Major phase	Minor phases
	Grey contrast	White contrast
0.00 Nd	$Ca_3Co_{3.68}O_9$	
0.01 Nd	$Ca_3Co_{3.66}O_9$	$Ca_3Nd_{0.02}Co_{2.3}O_9$
0.03 Nd	$Ca_3Co_{3.73}O_9$	$Ca_3Nd_{0.06}Co_{2.3}O_6$
0.05 Nd	$Ca_3Co_{3.7}O_9$	$Ca_3Nd_{0.1}Co_{2.4}O_6$

Figure captions:

Figure 1. Powder X-ray diffraction patterns obtained for the $Ca_{3-x}Nd_xCo_4O_y$ samples; x = 0.00 (a); 0.01 (b); 0.03 (c); and 0.05 (d). The diffraction planes indicate the $Ca_3Co_4O_9$ phase and the * the $Ca_3Co_2O_6$ ones. The # symbol identifies the (111) diffraction peak of Si, used as reference.

Figure 2. SEM micrographs performed on polished sections of $Ca_{3-x}Nd_xCo_4O_y$ samples; x = 0.00 (a); 0.01 (b); 0.03 (c); and 0.05 (d). Grey contrast (#1) corresponds to the $Ca_{3-x}Nd_xCo_4O_y$ phase; white one (#2) to the $Ca_{3-x}Nd_xCo_2O_6$.

Figure 3. Apparent density values of $Ca_{3-x}Nd_xCo_4O_y$ samples, together with their standard errors, as a function of Nd-content.

Figure 4. Temperature dependence of the Seebeck coefficient, as a function of Nd content, in $Ca_{3-x}Nd_xCo_4O_y$ samples, for x = 0.00 (●); 0.01 (◆); 0.03 (■); and 0.05 (▲).

Figure 5. Temperature dependence of the electrical resistivity, as a function of Nd content, in $Ca_{3-x}Nd_xCo_4O_y$ samples, for x = 0.00 (●); 0.01 (◆); 0.03 (■); and 0.05 (▲).

Figure 6. Ln (σT) *versus* $1/k_BT$ plot as a function of Nd content, in $Ca_{3-x}Nd_xCo_4O_y$ samples, for x = 0.00 (●); 0.01 (◆); 0.03 (■); and 0.05 (▲). The slopes of the fittings are nearly the same in all cases, below T*. T_1* and T_2*

indicate the metallic-to-semiconducting transition temperature for the Nd-doped samples and the pure ones, respectively. The insert shows a higher magnification view of the low temperature region.

Figure 7. Temperature dependence of the power factor, as a function of Nd content, in $Ca_{3-x}Nd_xCo_4O_y$ samples, for x = 0.00 (●); 0.01 (◆); 0.03 (■); and 0.05 (▲).

Figure 1

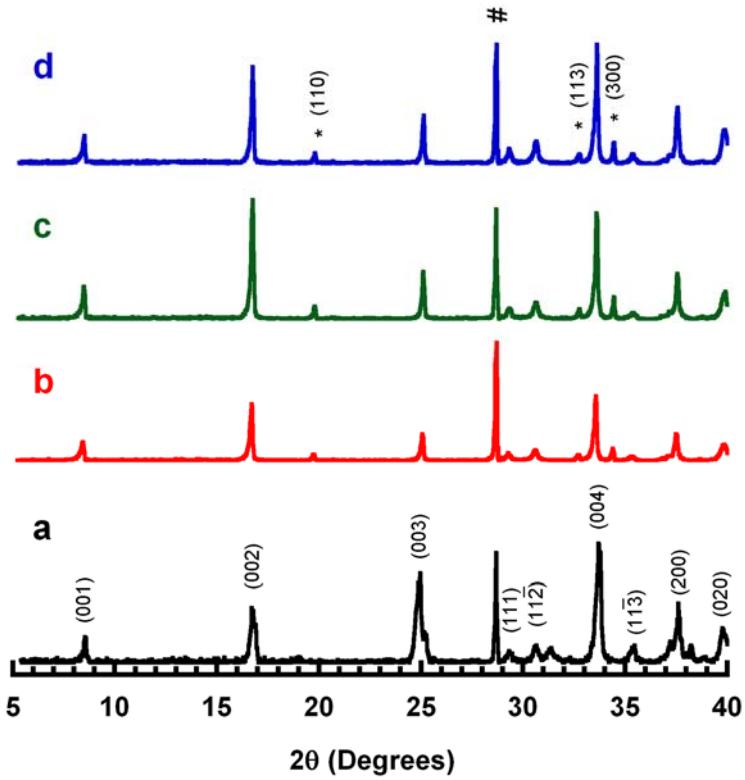
d
c
b
a
#
* (110)
* (113)
* (300)
(001)
(002)
(003)
(111)
(11$\bar{2}$)
(004)
(11$\bar{3}$)
(200)
(020)
5
10
15
20
25
30
35
40
2θ (Degrees)

Figure 2

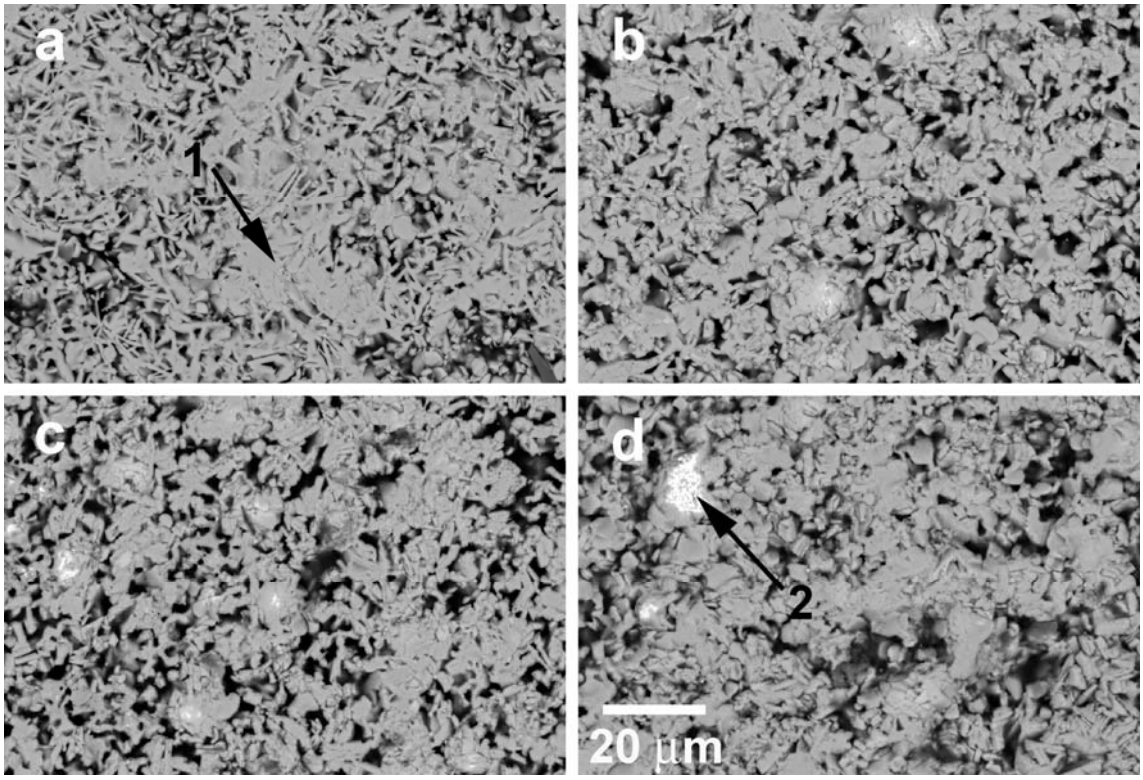

Figure 3

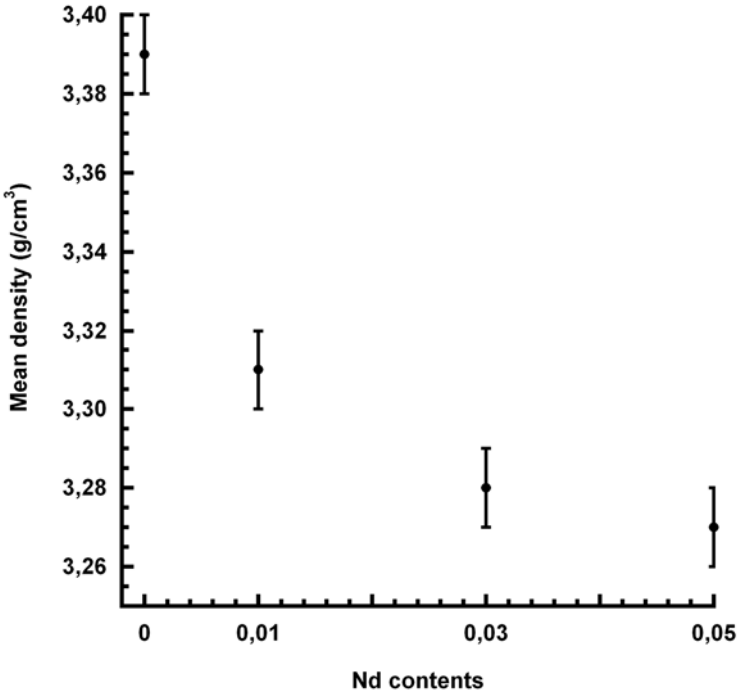
3,40
3,38
3,36
3,34
3,32
3,30
3,28
3,26
Mean density (g/cm3)
0
0,01
0,03
0,05
Nd contents

Figure 4

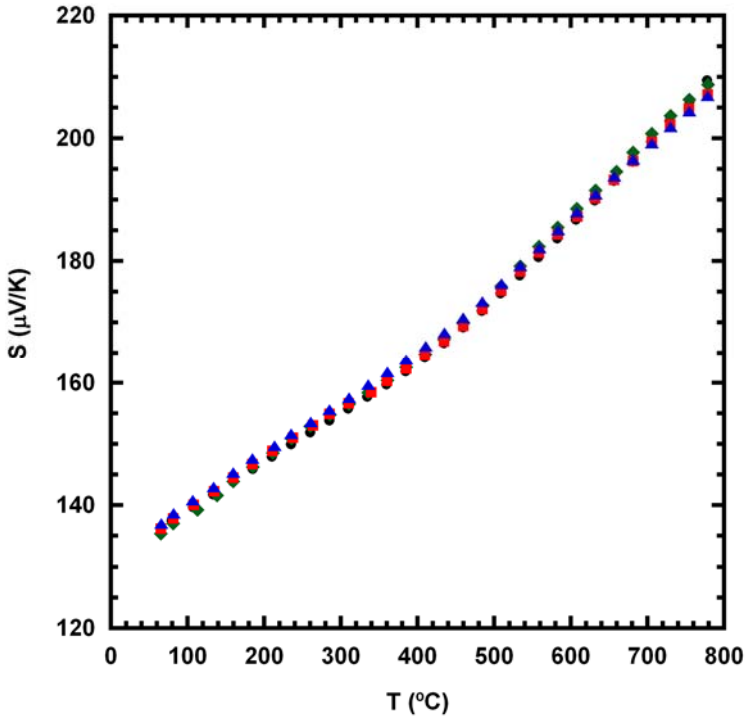

Figure 5

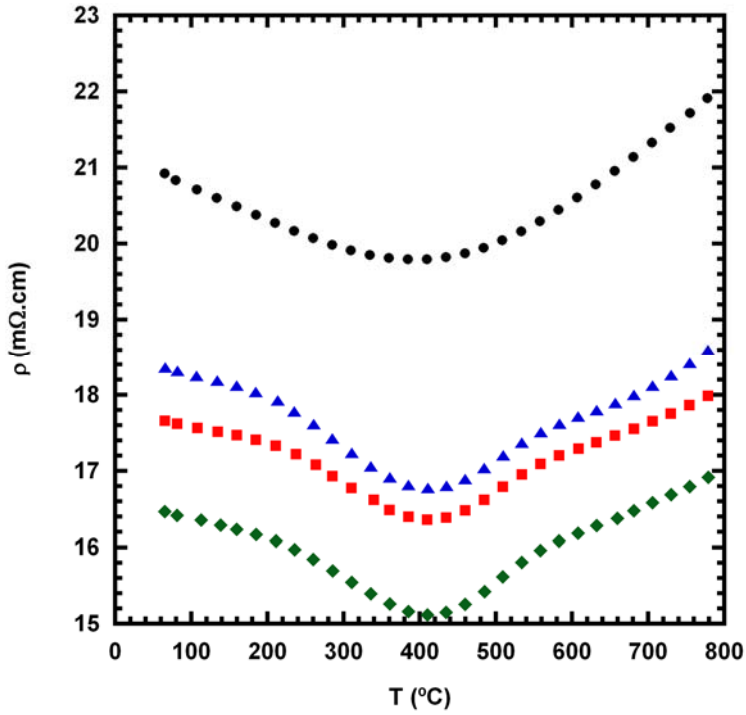
ρ (mΩ.cm)
T (°C)
23
22
21
20
19
18
17
16
15
0
100
200
300
400
500
600
700
800

Figure 6

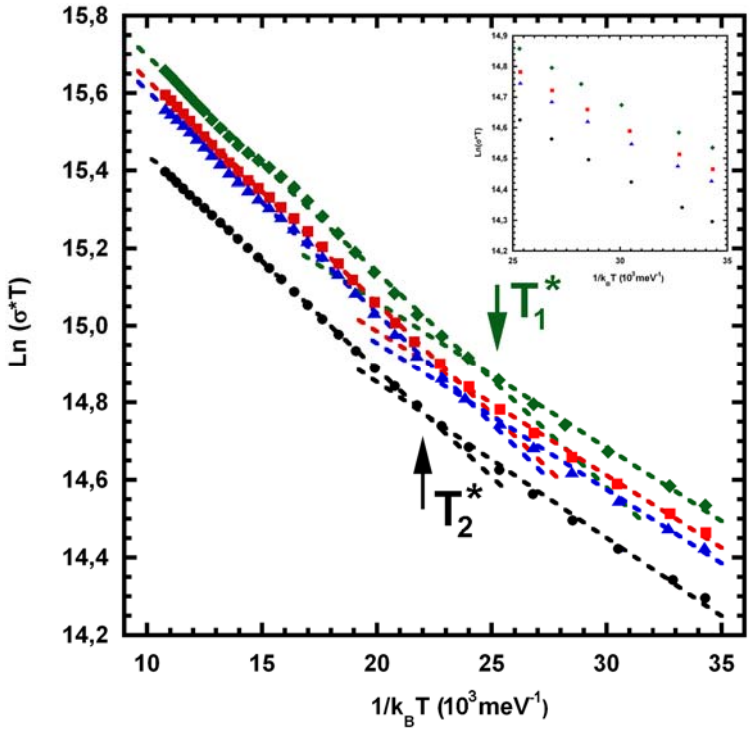
15,8
15,6
15,4
15,2
15,0
14,8
14,6
14,4
14,2
Ln (σ*T)
10
15
20
25
30
35
1/k_B T (10^3 meV^-1)
T1*
T2*

Figure 7

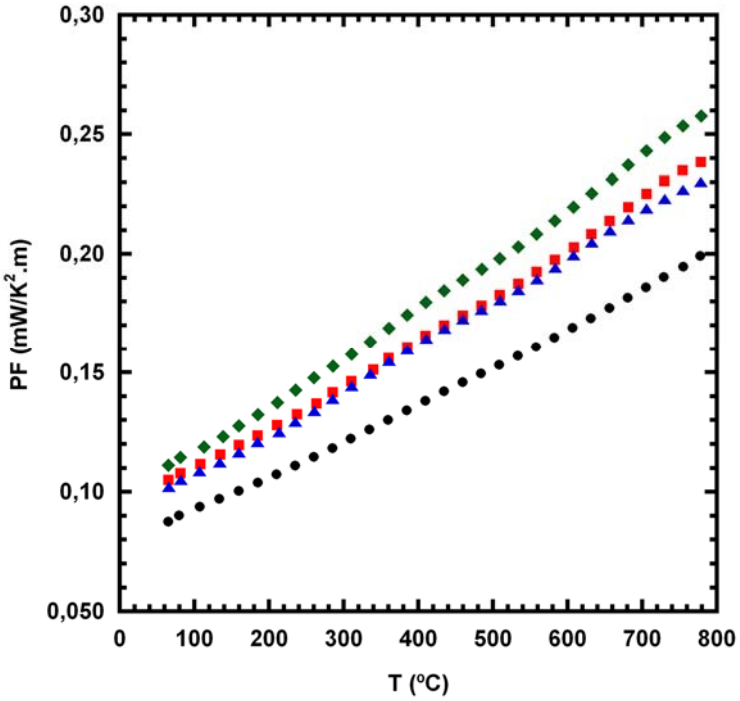
0,30
0,25
0,20
0,15
0,10
0,050
PF (mW/K².m)
0
100
200
300
400
500
600
700
800
T (ºC)